Development of a Wide-Band imaging FT-IR Spectrometer with Wavefront-Division Phase-Shift

Wide-band mid-infrared imaging spectroscopy in the 4–20 μm band is a key capability for planetary atmosphere and surface studies because molecular vibrational fingerprints can be mapped spatially at high throughput. Conventional imaging FT-IR approaches based on Michelson interferometry require a beamsplitter and long, mechanically stable optical-path-difference (OPD) scanning, which makes compact payload implementation difficult, particularly in the 4–20 μm band where transmissive optics and beamsplitters introduce strong material absorption and chromatic dispersion. To address these limitations, we develop a compact two-dimensional wavefront-division Fourier-transform infrared (2D WFT-IR) imaging spectrometer that is fully reflective and uses near-axis phase scanning with a plane-mirror pair.

The instrument concept is illustrated in Fig. 1. Fore optics form a real image of the scene on the entrance plane; a WPSM then selects spatial portions of the incident wavefront. The selected field is collimated by the first Zernike freeform mirror (M1) into plane waves that enter the wavefront-division delay line. Two gold-coated plane mirrors (P1 movable, P2 fixed) are placed side-by-side near the optical axis; a small normal displacement L of P1 generates an OPD of 2L cosα between the divided wavefront portions (α is the reflection angle). The OPD-encoded plane waves are reimaged by a second freeform mirror (M2) onto a wide-band uncooled mid-IR focal-plane array (FPA). Each detector pixel records an interferogram during a scan; a Fourier transform along the OPD axis reconstructs a spectrum per pixel, producing a hyperspectral cube in a single acquisition without slit scanning.

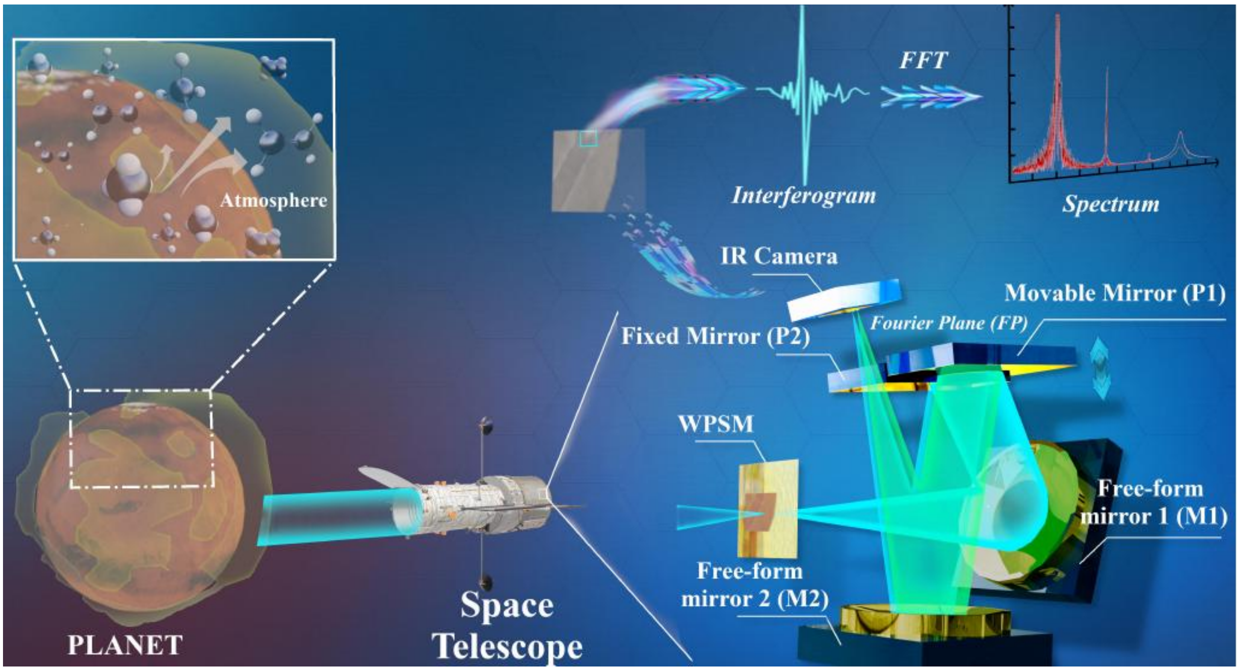

Fig. 1. Optical architecture of the wide-band 2D WFT-IR: fore optics → WPSM → Zernike freeform collimator (M1) → plane-mirror wavefront-division phase scanner (P1/P2) → freeform imager (M2) → IR FPA; per-pixel FFT yields spectra.

A central design goal is to realize diffraction-limited imaging over a wide rectangular field while leaving mechanical space for the phase scanner stroke. We therefore adopt a three-fold folded reflective geometry and describe each freeform mirror surface by a limited set of standard Zernike polynomial terms, enabling efficient aberration control during optimization (Fig. 2). Zemax modeling and multi-configuration analysis show that the design maintains spotsizes within the Airy disk across nine field points while the Fourier-plane (FP) position varies over the usable scan range. The final optical solution achieves an effective focal length of 85.89 mm with F/# = 1.93 and 2.38% distortion over a 10.8 × 8.2 mm field, with an overall footprint of approximately 110 × 94 mm (Fig. 2). A Monte Carlo tolerance analysis (1000 trials) with ±20 μm mechanical positioning errors and ≤1 μm PV surface figure error indicates robust manufacturability: ≥98% of trials satisfy acceptance criteria for RMS spot radius (<17 µm), RMS wavefront error (<0.07λ at 4 µm), and MTF at 29 lp/mm (>0.10).

The system uses a near-axis wavefront-division phase-scanning method to record spectra at each pixel in a 2D image. When a plane wave reaches the delay line, two portions of the wavefront are separated near the optical axis.

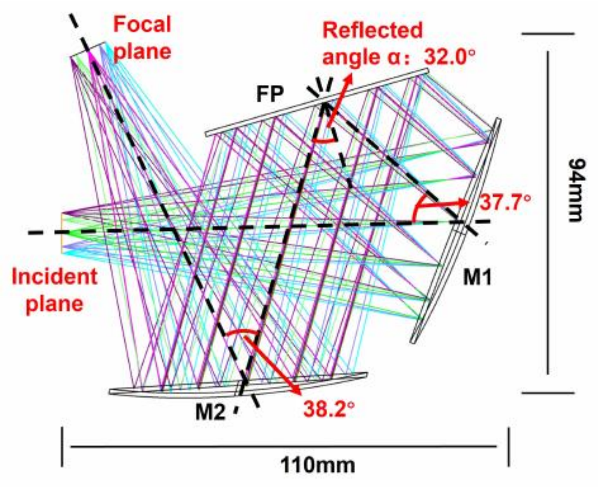

Fig. 2. Folded three-mirror reflective imaging train optimized with Zernike freeform surfaces (M1/M2). The folded geometry keeps the system compact while preserving diffraction-limited imaging over the field.

One part reflects from a fixed mirror, while the other reflects from a mirror that moves along its normal direction. A mirror displacement L produces an OPD of $2L\cos\alpha$, where α is the reflection angle. The field at a detector pixel (x,y) can be written as

$$I(x,y,L) = I_0(x,y)[1 + V(x,y)\cos\phi(x,y;L)] \tag{1}$$

where I_0 is a slowly varying intensity term, V is the fringe visibility, and the phase is

$$\phi(x,y;L) = {}^{4\pi}\!/_{\lambda}\, L\cos\alpha + \phi_0(x,y) \tag{2}$$

During a mirror scan, the detector records $I(x,y,L)$ for all pixels, and a Fourier transform along the L- axis retrieves a spectrum for each pixel, producing a hyperspectral image in a single acquisition. This phase -shifting wavefront- division method maintains compact geometry, eliminates the need for a beamsplitter, and provides strong vibration robustness because most of the optical path is shared.

In a wavefront- division interferometer, the loss of fringe visibility arises not from temporal coherence but from the limited spatial coherence of an extended source. When the source has a finite angular width, light from its two edge regions produces interference patterns that are shifted by approximately one fringe period. As illustrated in Fig. 3(a), the 0th- order bright fringe from one edge overlaps the ±1st- order dark fringe from the opposite edge, while the contribution from the central region lies between them. Because these contributions are mutually incoherent, their intensities add at the detector, the dark fringes become filled, and the measurable fringe contrast collapses. In a 1D approximation, the Van Cittert–Zernike theorem yields a critical source width

$$W_{\text{source}} = \bar{\lambda}\,\frac{f_{\text{obj}}}{d} \tag{3}$$

where $\bar{\lambda}$ is the mean wavelength, $f$obj is the focal length of the collimating optics, and d is the baseline between the two divided wavefronts. Preserving contrast requires $W_{\text{open}} < W_{\text{source}}$, while avoiding excessive slit diffraction imposes $W_{\text{open}} > \lambda_{max}(F/\#)$. In 2D, the mask becomes a periodic slit array; to avoid lateral bright–dark mixing between adjacent object points, the period must exceed the radius containing ~95% of the Airy energy at the longest wavelength,$P > r_{\text{Airy-95¥\%}} = 1.616\,\lambda_{max}(F/\#)$. Finally, to suppress moiré-type phase drifts caused by mismatch

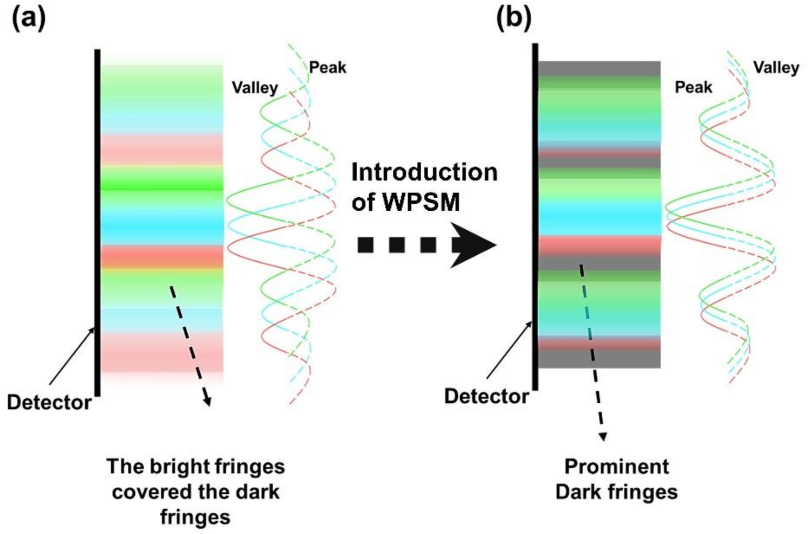

Fig. 3. Restoring interference contrast with the WPSM. (a) Without WPSM, a wide source sends light from both edges, and the bright fringes from one edge (red) fall onto the dark fringes from the other edge (green). The central part (blue) lies between them, causing dark fringes to be filled. (b) With WPSM, the outer source regions are blocked so that only the central portion of the wavefront passes. Bright and dark fringes again aging, restoring clear contrast across the field.

between the slit pitch and the detector pixel grid, we enforce integer-multiple constraints

$$W_{\text{final}} = kp, \qquad P_{\text{final}} = mp, \qquad k, m \in Z \tag{4}$$

For our optics (F/# ≈ 1.9) these constraints define an allowable opening window of roughly 47–69 µm; the nearest integer multiple is W = 4p = 68 µm, and we fabricate a 68:68 µm (open: block) WPSM on a 150 µm-thick Si wafer by Bosch deep reactive-ion etching. As shown in Fig. 3(b), this geometry effectively suppresses fringe mixing from extended sources while maintaining high imaging quality across the field, enabling strong and spatially uniform interference contrast in the 2D WFT-IR system.

We correct this by mapping each pixel's OPD to a common reference before Fourier transformation using $\theta x = tan^{-1}(x/f)$ and $\theta y = tan^{-1}(y/f)$, and refining α as a fit parameter to minimize field-wide spectral offsets. Using a monochromatic quantum cascade laser (QCL, $\nu\tilde{0}$= 960 cm^{-1}, linewidth ≤0.1 cm^{-1}) and synchronized acquisition (50 Hz camera; 50 µm/s piezo scan) we record ~2000 frames per scan over a mirror stroke ΔL = 2 mm. The theoretical central wavenumber resolution is$\Delta\nu_{\tilde{t}heory} = 1/(2\Delta Lcos\alpha) \approx 2.95cm^{-1}$. Experimentally, Gaussian fits to the reconstructed QCL line yield FWHM values of 4.28 cm^{-1} (top), 3.62 cm^{-1} (center), and 3.66 cm^{-1} (right), giving a mean $\Delta\tilde{\nu} \approx 3.85$ cm^{-1}, in good agreement with the theoretical limit. After full-field OPD correction on 217,707 valid pixels in an 8×8 mm^2 region, residual peak-position offsets form a narrow distribution with mean 0.0504 ± 0.0110 cm^{-1} (95% CI) and standard deviation 2.42 cm^{-1}, confirming high wavenumber accuracy relative to the ~4 cm^{-1} system resolution.

Spatial imaging performance is evaluated with a USAF resolution target under 950°C filament illumination. The finest resolved element is Group 4, Element 6 (14.3 lp/mm), for which edge-based analysis indicates a measured line width of two pixels (≈34.0 µm), consistent with the chart's theoretical 34.96 µm feature size and with the diffraction-limited design constraints at the short-wavelength end. These measurements establish a practical spatial resolution of approximately 35 µm, close to the 2×17 µm pixel sampling limit and suitable for two-dimensional chemical mapping in compact payload geometries.

To assess whether the reconstructed two-dimensional spectral maps remain consistent across the field—an essential requirement for quantitative imaging spectroscopy—we measure a certified polystyrene (PS) reference film using a wide-band lamp and a simple front-end focusing optics. Spectra are reconstructed over 500–2800 cm^{-1}

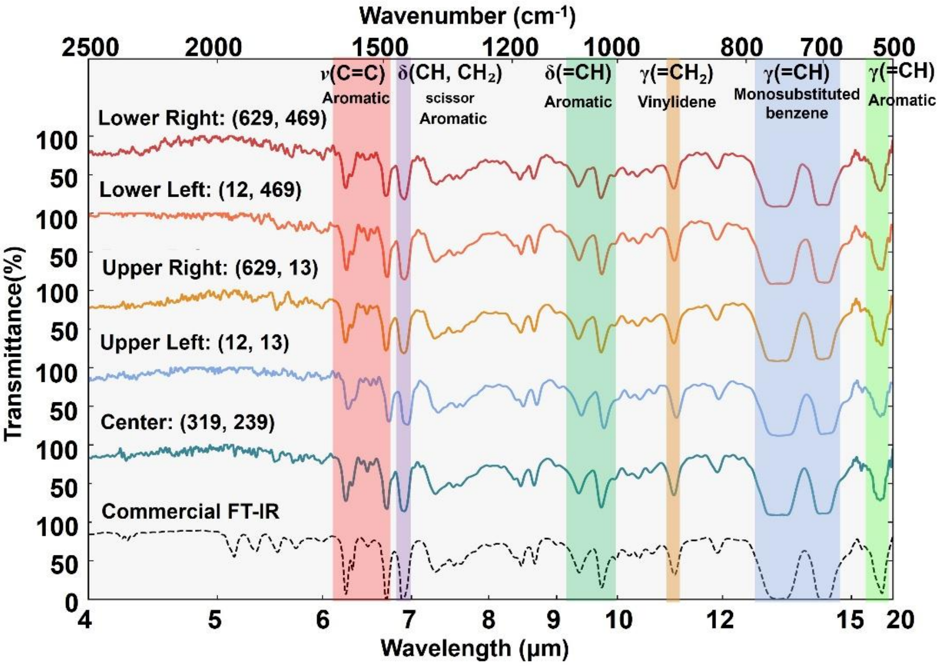

Fig. 4. Polystyrene transmittance spectra reconstructed at five field positions (20×20-pixel averages) compared with a commercial FT-IR reference. Peak positions and shapes remain consistent across the image.

and averaged over 20×20-pixel blocks in five regions (center and four corners). As shown in Fig. 4, the spectral baselines, peak shapes, and characteristic absorption bands agree closely across all regions and match a commercial FT-IR reference (JASCO FT/IR-6100). The standard deviation of peak positions among the five regions is 2.73 cm^{-1} (center), 3.71 cm^{-1} (upper left), 2.45 cm^{-1} (upper right), 3.34 cm^{-1} (lower left), and 2.43 cm^{-1} (lower right). These spreads are comparable to the intrinsic spectral resolution, indicating that the OPD correction and imaging optics together maintain field-wide spectral uniformity so that 2D spectral maps are spatially consistent within the system's resolving power.

A key challenge in wavefront-division interferometry is that fringe visibility can collapse for extended sources due to limited spatial coherence: light from different incident angles generates fringe systems that are shifted relative to each other, and incoherent superposition fills dark fringes (Fig.5(a)). In our experiments, removing the WPSM results in an interferogram with no clear zero-path-difference (ZPD) burst and fringe amplitude near the noise floor; inserting the WPSM increases the fringe peak by ~50× and improves fringe contrast by ~97.7%, enabling reliable phase alignment, cyclic shifting, and apodization in the Fourier reconstruction (Fig.5(b)). The WPSM therefore plays a dual role: it restores interferometric contrast and ensures that the recorded interferograms remain valid Fourier data rather than incoherent intensity sums.

With the integer-matched 68:68 μm design, interferograms extracted from multiple pixels along the central column exhibit nearly identical fringe shapes and aligned ZPD positions, demonstrating spatial stability without position-dependent phase inversion. As shown in the Fig.5(c), the ZPD peak amplitude decreases from the center (~2750 counts) to intermediate positions (~2000 counts) and to the field edges (~1000 counts). This "bright-center, dim-edge" trend is consistent with a cosine-fourth illumination law combined with field vignetting in the front-end optics, $A_{\text{ZPD}}(\theta_y) \propto I_0 \cos^4 \theta_y \;\; V_{\text{vig}}(\theta_y)$, rather than a loss of coherence; thus, fringe visibility remains nearly uniform while overall irradiance varies with field angle. Practically, this correlation between intensity and interferogram amplitude clarifies that improving illumination uniformity (e.g., telecentric fore optics and reduced vignetting) can raise SNR at the edges without sacrificing coherence once the WPSM geometry is properly matched to the sampling grid.

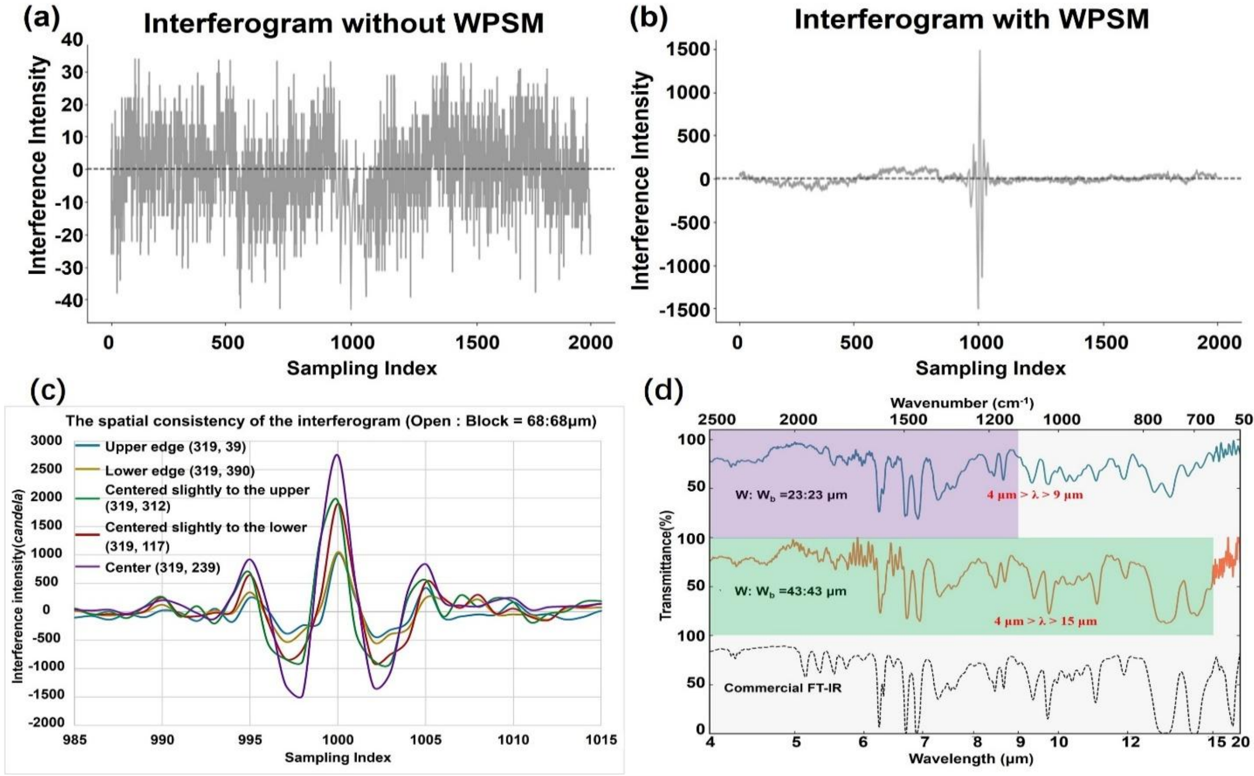

Fig. 5. (a) Interferograms obtained with the 2D WFT-IR without WPSM, dominated by incoherent mixing; (b) with WPSM, showing a strong zero-path-difference (ZPD) burst and enhanced fringe contrast; (c)Interferograms extracted from five pixel positions along the central detector column for the 68 μm:68 μm WPSM;(d)PS absorption spectra measured using WPSMs with different widths.

The WPSM width also imposes a fundamental trade-off between coherence control and usable spectral bandwidth. When the opening is too narrow, diffraction at the slit spreads long-wavelength radiation over a wider angular range such that a significant fraction does not reach the detector or does not interfere efficiently, acting as an effective long-wavelength cut-off. We verify this experimentally by measuring PS spectra with WPSMs of 43:43 μm and 23:23 μm under identical conditions. As summarized in Fig. 5(d), the 43 μm design restricts the detectable band to ~4–15 μm, whereas the 23 μm design further contracts the usable band to ~4–9 μm. In contrast, the selected 68 μm WPSM maintains broadband response comparable to the commercial reference up to ~20 μm, demonstrating that a WPSM optimized for spatial coherence must also respect diffraction-limited throughput at the longest wavelengths.

In conclusion, this work developed a compact imaging FT-IR spectrograph that combines near-axis wavefront-division interferometry with Zernike freeform reflective optics to enable wide-band operation across 4–20 μm. The two freeform mirrors provide aberration-controlled collimation and imaging, while the Wavefront Pre-Selection Mask (WPSM) manages spatial coherence by limiting the angular extent of the extended source, preventing bright–dark fringe overlap that normally suppresses visibility in wavefront-division systems. With the optimized WPSM geometry, the fringe amplitude increases by nearly 50× and the contrast improves by about 97.7%, enabling a wavenumber resolution of ~ 3.6 cm−1 and a spatial resolution of ~ 34 μm in a compact all-reflective layout. Field-wide measurements using a JASCO PS standard confirm that peak positions and band shapes remain consistent with those of a commercial FT-IR reference at both the center and corners of the image, demonstrating stable spectral accuracy and uniformity. These results show that the combination of Zernike freeform optics, wavefront-division interferometry, and the WPSM offers an effective and mechanically robust approach to high-contrast, wide-band mid-infrared imaging spectroscopy, providing a practical pathway toward small, high-performance FT-IR instruments suitable for both laboratory and spaceborne applications.